Rottier, B., Chelle-Michou, C., Casanova, V., Pastore, C., and Tollan, P., 2023, Early Au-rich sulfide liquid saturation explains the low Au endowment of continental intraplate alkaline magmas: Geology, v. 50, https://doi.org/10.1130/G50515.1

SUPPLEMENTARY MATERIAL

CONTENTS

Location of the samples (Fig. S1)

The Banne d'Ordanche summit is located 5 km Nord West of the city of La Bourboule (France). The GPS coordinates (UTM WGS84) of the samples are:

BR-03: 45°36'40.5"N 2°45'52.1"E

BR-04: 45°36'40.9"N 2°45'57.2"E

BR-06: 45°36'39.1"N 2°46'14.6"E

BR-07: 45°36'41.8"N 2°46'15.8"E

BR-08: 45°36'26.3"N 2°45'36.0"E

BR-09: 45°36'26.6"N 2°45'33.7"E

BR-10: 45°36'26.7"N 2°45'32.2"E

BR-11: 45°36'26.6"N 2°45'30.9"E

BR-12: 45°36'26.7"N 2°45'29.9"E

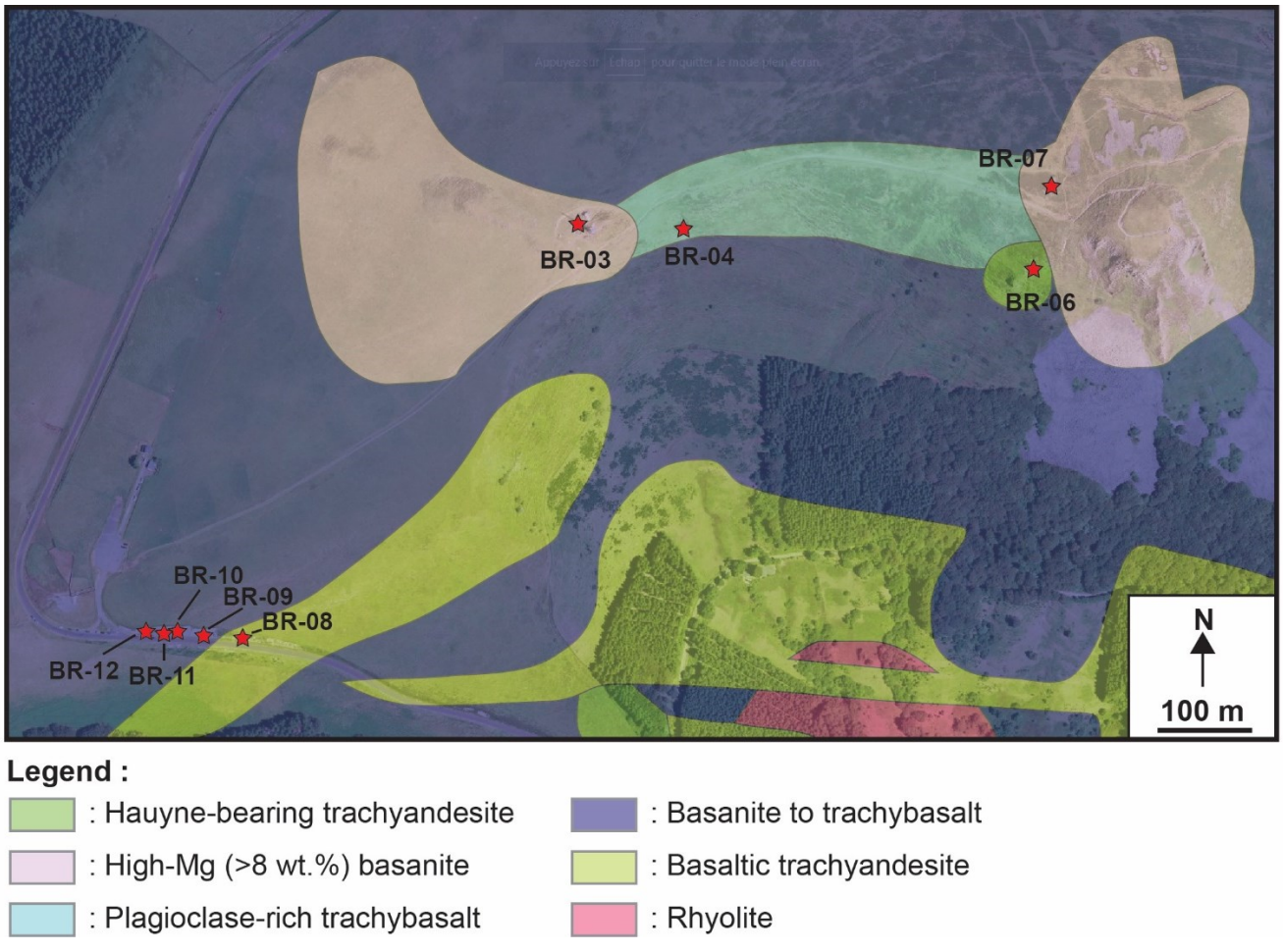

Figure S1: Simplified geological map of the Banne d'Ordanche summit (modified from Brousse and Tempier (1981)) showing the position of the samples used in this study.

Whole Rock Geochemistry (Fig. S2)

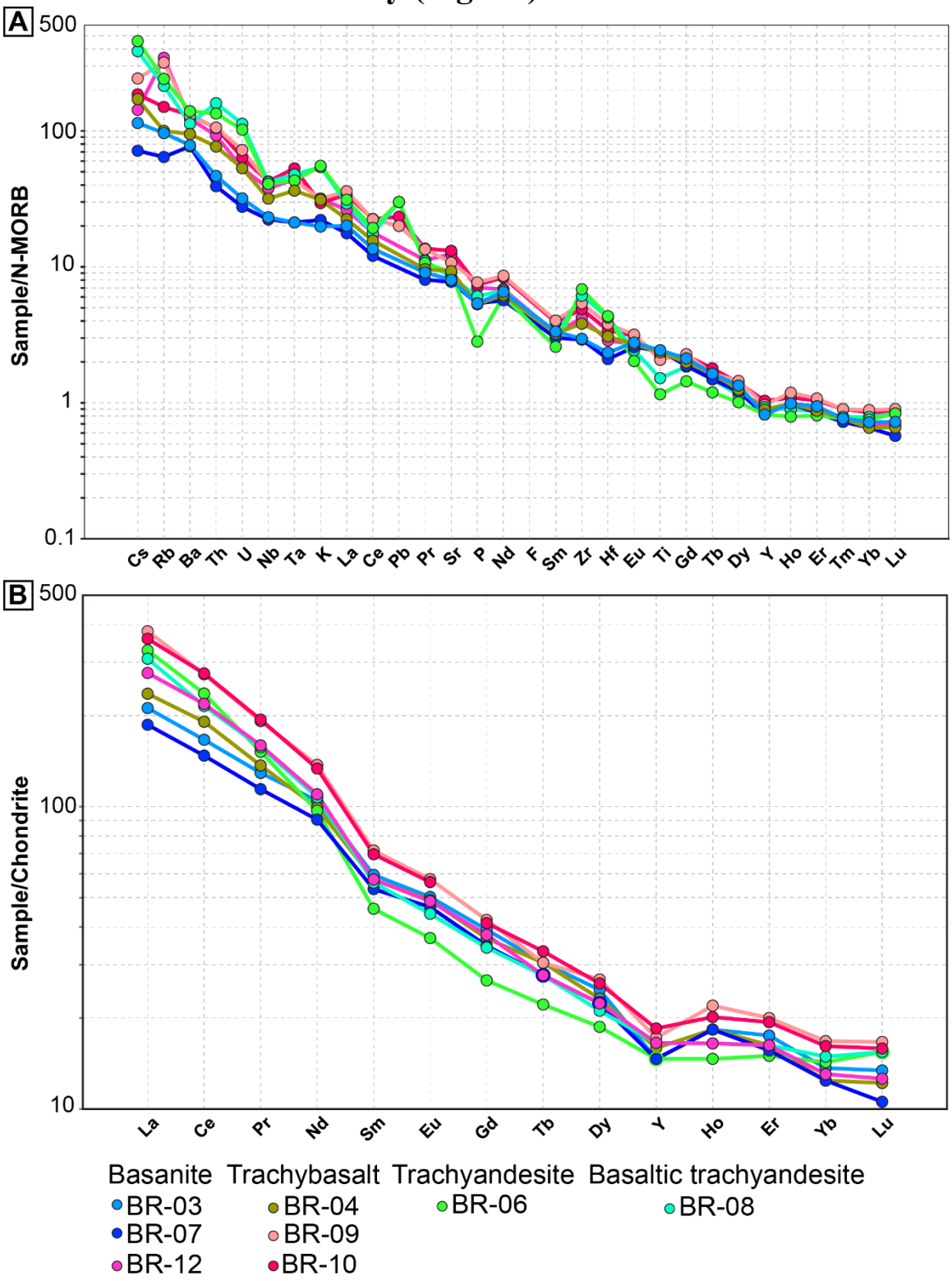

Figure S2: (A) N-MORB-normalized trace element spider diagrams (Sun and McDonough,1989); (B) Chondrite-normalized REE patterns (McDonough and Sun,1995)

Additional data on the silicate melt inclusions (Fig. S3)

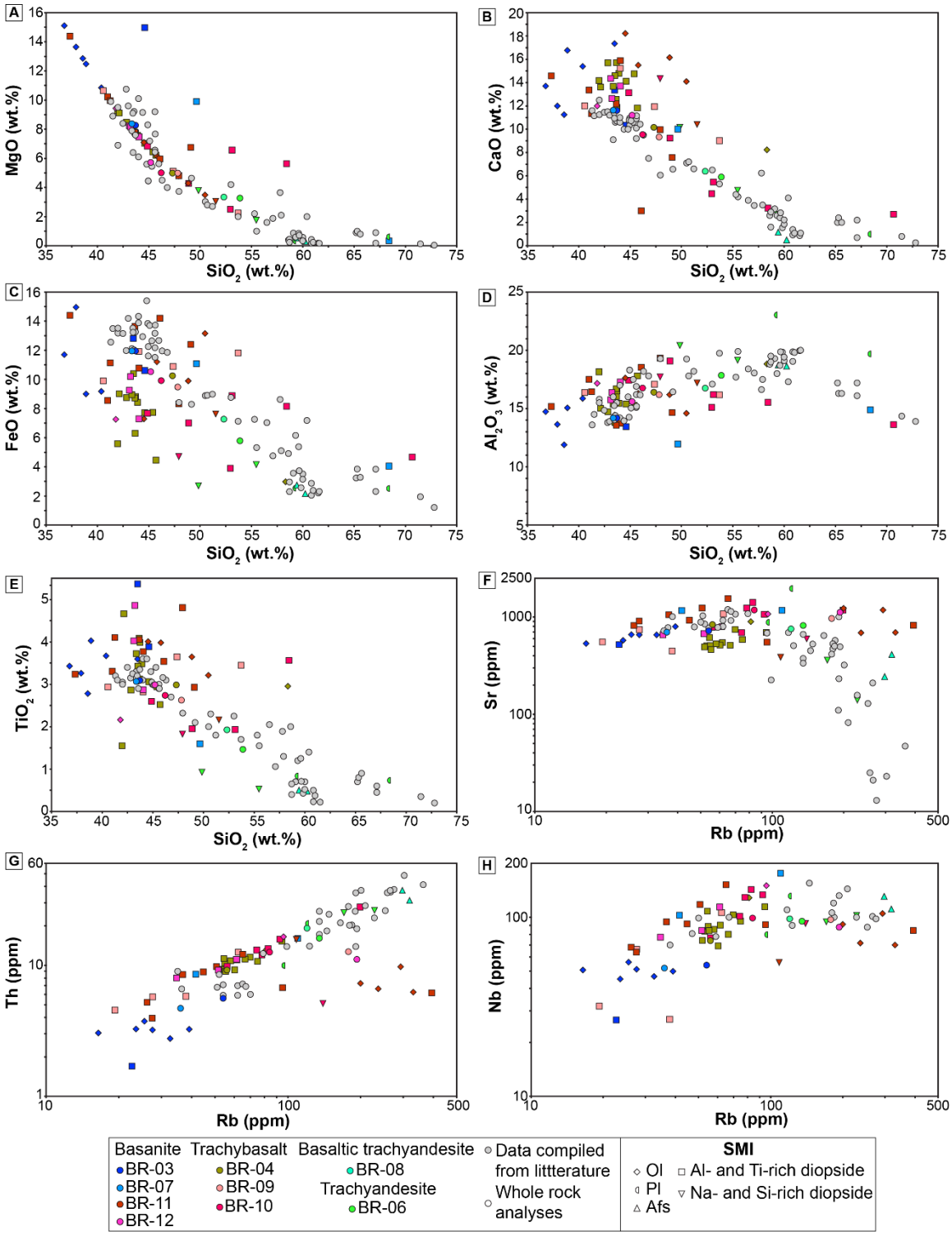

Figure S3: Major and trace elements composition of the whole rock and the silicate melt inclusion. A) MgO vs. SiO_2; B) CaO vs. SiO_2; C) FeO vs. SiO_2; D) Al2O3 vs. SiO_2; E) TiO_2 vs. SiO_2; F) Sr vs. Rb; G) Th vs. Rb; H) Nb vs. Rb

Additional data on the magmatic sulfide inclusions

Description (Fig. S4)

Exposed magmatic sulfide inclusions have been observed in Al- and Ti-rich diopside, Kaersutite and magnetite. Abundance, size, and the mineral phases observed in magmatic sulfide inclusions hosted in magnetite are similar than those observed in Al- and Ti-rich diopside and Kaersutite. Most exposed magmatic sulfide inclusions are rounded, between < 10 µm and up to 60 µm, occurs mostly isolated and few formed groups restricted to a growth zone of their host phenocrysts (Fig. S4 A-H). They are dominated by pyrrhotite, almost always a small amount of chalcopyrite is observed at the edge of the inclusions (Figs. S4 A), and in rare case magnetite is observed too (Figs. S4 B). Exposed magmatic sulfide inclusions present in or close to cracks are partly oxidized probably due to weathering or due to late degassing emplacement of the lava flows.

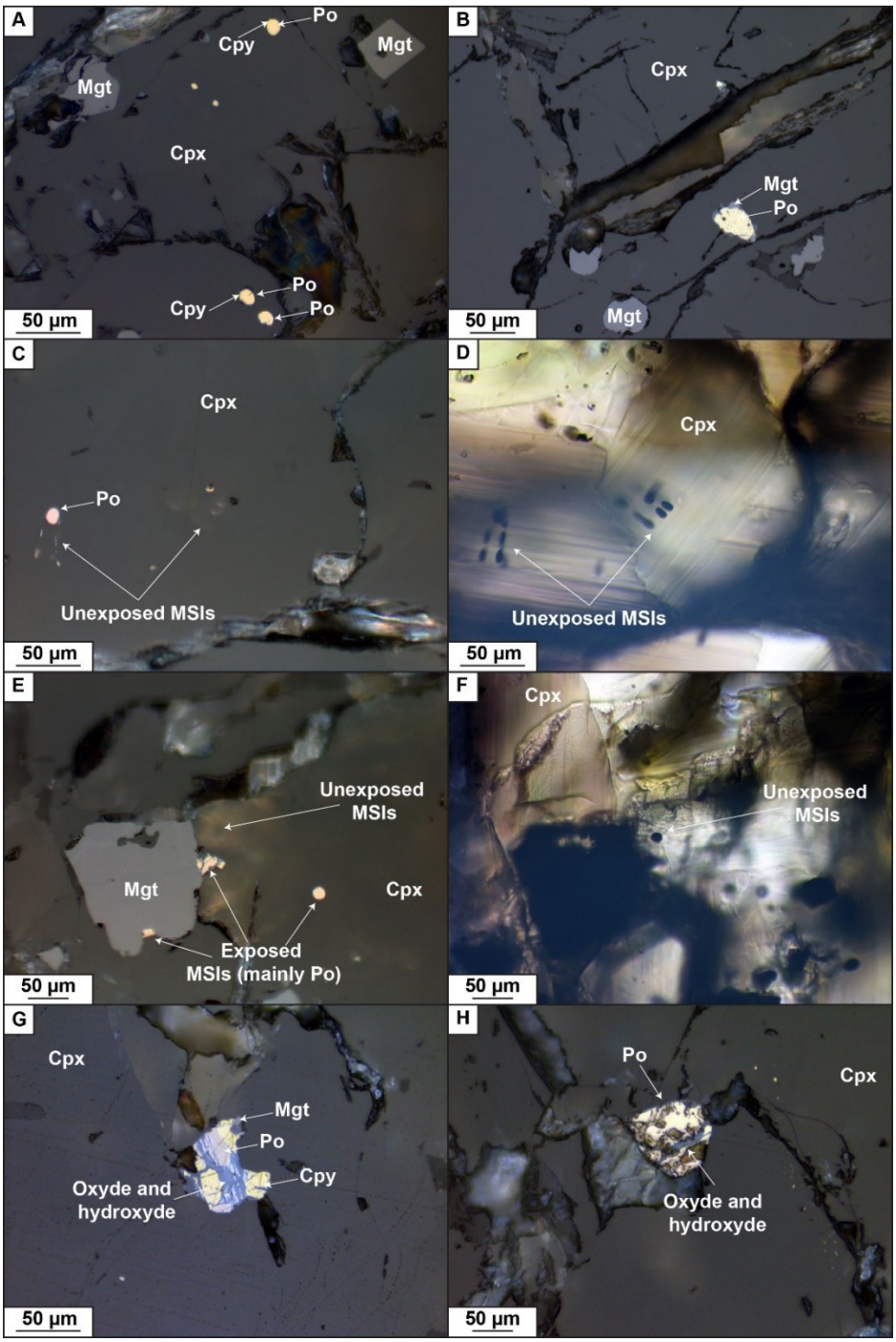

Figure S4: Microphotographs of exposed and unexposed magmatic sulfide melt inclusions hosted in Al- and Ti-rich diopside. A) Reflected light photography of several exposed MSIs formed by pyrrhotite with a tiny rim of chalcopyrite in sample BR-11. B) Reflected light photography of exposed MSI mainly composed of pyrrhotite with small magnetite grains at the border in sample BR-11. C) Reflected light photography of two exposed MSIs mainly formed by pyrrhotite from sample BR-03. D) Same picture than D in transmitted light showing the unexposed MSIs. E) Reflected light photography of several exposed MSIs mainly formed by pyrrhotite from sample BR-03. F) Same picture than E in transmitted light showing an unexposed MSI. G) Exposed MSI formed by pyrrhotite, chalcopyrite, and magnetite partly altered to iron oxides and hyroxides from sample BR-07. H) Exposed MSI formed by pyrrhotite partly altered to iron oxides and hyroxides from sample BR-09.

Nickel content of the MSIs as tracer of magmatic differentiation (Figs. S5 and S6)

Several studies have shown that Ni content of magmatic sulfide inclusions is a good tracer of the evolution of the residual melt (e.g., Rottier et al., 2020; Chang and Audétat 2021; Du and Audétat 2020). In this study, this statement appears is supported by the following data. First, in 6 Al- and Ti-rich diopside phenocrysts both silicate melt and magmatic sulfide melt inclusions have been analyzed. The Ni content of the MSIs is positively correlated with compatible elements (e.g., TiO_2; Fig. S4) and negatively correlated with incompatible elements (e.g., Pb and Cs; Figure S4). Secondly, the Ni content of the MSIs is correlated with the chemical composition of their host phenocrysts (Al- and Ti-rich diopside and Kaersutite). The Ni content of the MSIs decrease with the Ni content of their host Al- and Ti-rich diopside (Fig. S5) which is a good tracer of the differentiation of the silicate melt. For Kaersutite, the Ni content of the MSIs decrease with the increase of the Mn content of the Kaersutite known to be enriched in amphibole during magmatic differentiation. These observations combined with the previous studies confirmed that the Ni content of MSIs can be used as a tracer of the evolution of the residual melt.

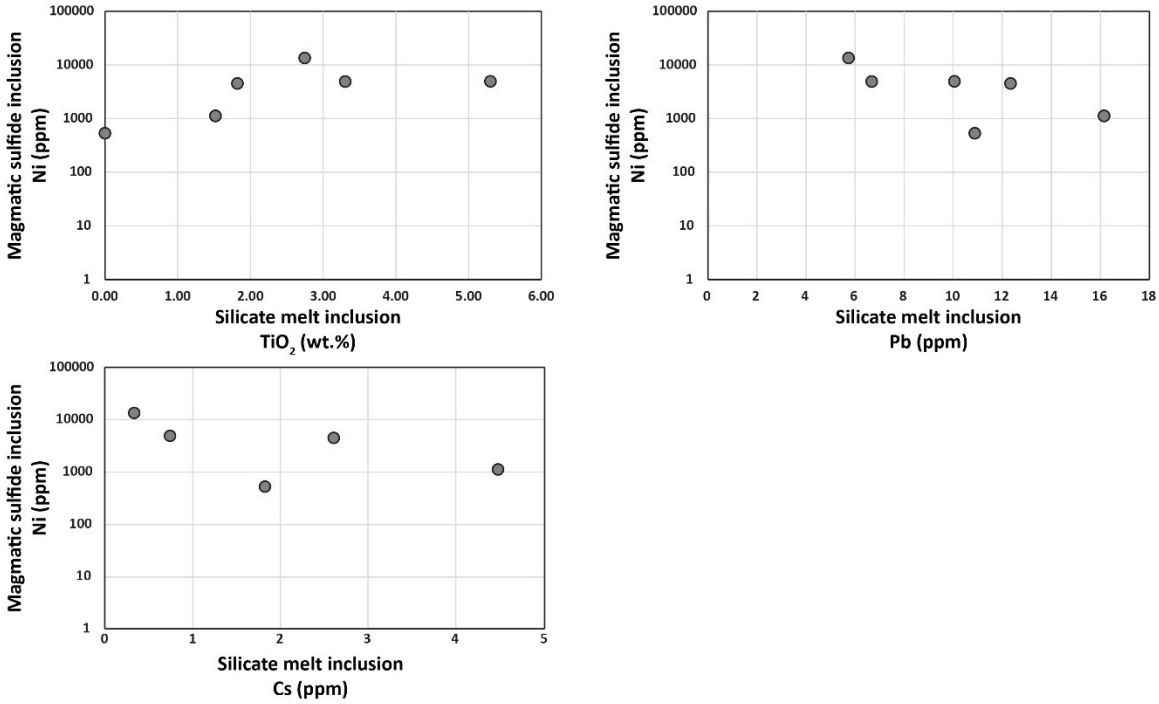

Figure S5: Comparison of the Ni content of analyzed MSIs and chemical composition of the silicate melt inclusions hosted in the same Al- and Ti-rich diopside phenocryst.

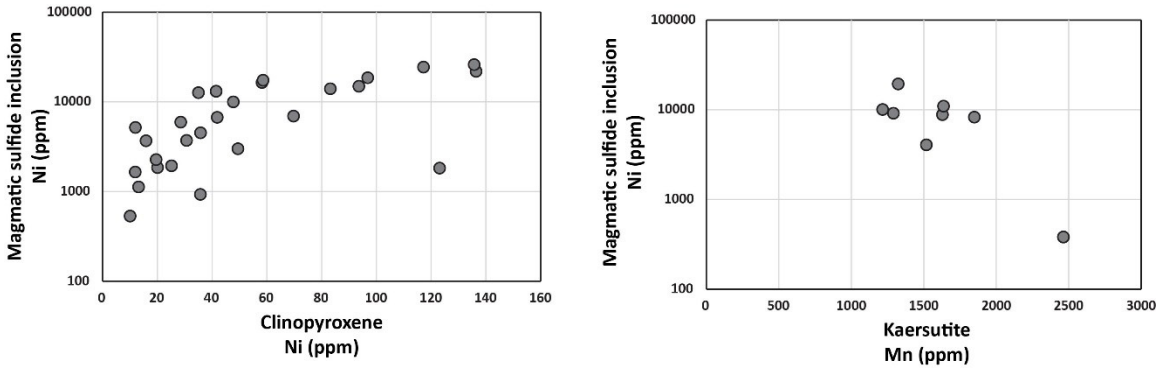

Figure S6: Comparison of the Ni content of analyzed MSIs and chemical composition of their host phenocrysts (Al- and Ti-rich diopside and Kaersutite).

Chemical composition of MSIs compared to literature data (Fig. S7)

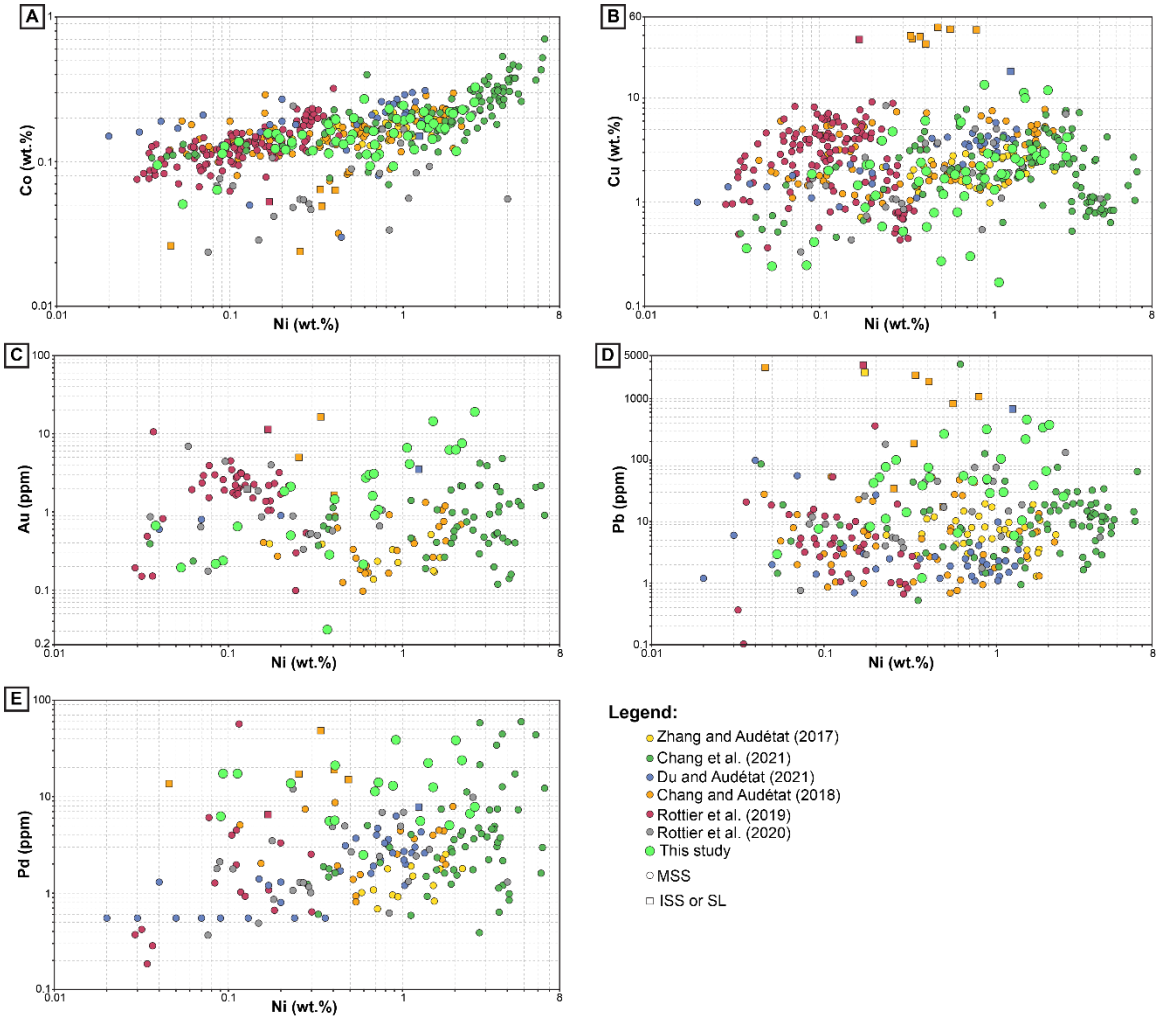

Figure S7: Comparison of the LA-ICP-MS analyses of magmatic sulfide inclusions from this study with literature data. A) Co vs. Ni; B) Cu vs. Ni; C) Au vs. Ni D) Pb vs. Ni; E) Pd vs. Ni.

Analytical Methods

EPMA

EPMA analyses of clinopyroxene, olivine, Cr-spinel plagioclase, kaersutite, alkali feldspar, ilmenite and magnetite were performed at the Université Laval (Québec, Canada) using a CAMECA SX-100 equipped with 5 spectrometers, using 15kV, 15 nA and a beam of 5 to 10 µm.

For the clinopyroxene: Na, Si, Mg, Al, K, Ca, Ni and Mn were measured for 20s on peak and on background; Fe, Cr and Ti were measured for 15s on peak and on background. Standardization was performed on albite (Na), quartz (Si), magnesium oxide (Mg), plagioclase (Al), diopside (Ca), orthoclase (K), hematite (Fe), chromite (Cr), rutile (Ti), nickeline (Ni) and rhodochrosite (Mn).

For the olivine: Na, Si, Mg, Al, Ti, Ca, Fe and Mn were measured for 20s on peak and on background; Cr, Co and Ni were measured for 15s on peak and on background. Standardization was performed on albite (Na), quartz (Si), magnesium oxide (Mg), plagioclase (Al), rutile (Ti), diopside (Ca), garnet (Fe), rhodochrosite (Mn), nickeline (Ni) and metal cobalt (Co).

For the Cr-spinel: Na, Mg, Al, Si, Ti, Fe, Cr, Co, Nb, V, and Ni were measured for 20s on peak and on background; Ca and Mn were measured for 15s on peak and on background. Standardization was performed on albite (Na), quartz (Si), magnesium oxide (Mg), plagioclase (Al), rutile (Ti), diopside (Ca), hematite (Fe), chromite (Cr), metal cobalt (Co), rhodochrosite (Mn), nickeline (Ni), metal niobium (Nb) and metal vanadium (V).

For the kaersutite: F, Si, Cl, Fe and Mn were measured for 20s on peak and on background; Na, Al, Mg, K, Ca, Cr, Ti, Co, Ni and P were measured for 15s on peak and on background. Standardization was performed on fluorite (F), albite (Na), quartz (Si), magnesium oxide (Mg), plagioclase (Al), orthoclase (K), Tugtupite (Cl), rutile (Ti), diopside (Ca), hematite (Fe), chromite (Cr), metal cobalt (Co), rhodochrosite (Mn), nickeline (Ni) and apatite (P).

For the plagioclase and alkali feldspar: Ca, K, Ti, Mn, Fe, and Ba were measured for 20s on peak and on background; Si, Al, Mg, Na, P, and Sr were measured for 15s on peak and on background. Standardization was performed on albite (Na), magnesium oxide (Mg), plagioclase (Al and Si), orthoclase (K), rutile (Ti), diopside (Ca), hematite (Fe), rhodochrosite (Mn), celestine (Sr), barite (Ba) and apatite (P).

For the ilmenite and magnetite: Na, Mg, Al, Si, Ti, Ca, Cr, Co, Mn, and P were measured for 20s on peak and on background; Ni and Fe were measured for 15s on peak and on background; V was measured for 30s on peak and on background. Standardization was performed on albite (Na), quartz (Si), magnesium oxide (Mg), plagioclase (Al), rutile (Ti), diopside (Ca), hematite (Fe), chromite (Cr), metal cobalt (Co), rhodochrosite (Mn), nickeline (Ni), metal niobium (Nb), metal vanadium (V) and apatite (P).

LA-ICP-MS

Unexposed silicate melt inclusions, sulfide inclusions, and their host minerals were analyzed by laser ablation inductively coupled-plasma mass spectrometry (LA-ICP-MS) at ETH Zurich. The utilized system consists of a 193 nm ArF Excimer laser attached to a quadrupole mass spectrometer (Elmer Nexion2000). The sample chamber was flushed with He gas at a rate of 1.0 l/min, to which 5 ml/min H_2 gas was added on the way to the ICPMS.

For the silicate melt inclusions, the laser was operated at 10 Hz and an energy density 15-20 J/cm2 on the sample surface using laser pits ranging from 20 to 80 μm in diameter. The analyzed isotopes include ^{7}Li, ^{23}Na, ^{25}Mg, ^{27}Al, ^{30}Si, ^{31}P, ^{39}K, ^{43}Ca, ^{49}Ti, ^{51}V, ^{55}Mn, ^{57}Fe, ^{62}Ni, ^{65}Cu, ^{66}Zn, ^{85}Rb, ^{88}Sr, ^{89}Y, ^{90}Zr, ^{93}Nb, ^{98}Mo, ^{109}Ag, ^{133}Cs, ^{137}Ba, ^{208}Pb, ^{232}Th and ^{238}U. A dwell time of 10 ms was used for all elements excepted for Cu (20 ms) and Ag (30 ms). The GSD-1G and NIST SRM 610 glasses were used as primary and secondary external standard, respectively. Entire, unexposed silicate melt inclusions were drilled out of the silicate host, and excess ablated host was subtracted numerically from the resulting LA-ICP-MS signals until the constraint for the internal standard was matched (Halter et al. 2004; Pettke 2006). Internal standardization was based on chemical trends displayed by whole-rock data from this study and the literature (Besson, 1978; Chauvel and Jahn 1980, Gourgaud et al., 1980; Briot et al., 1991; Sorensen et al., 1999). The SiO_2 vs. MgO trend was used for most SMIs hosted in olivine and clinopyroxene, the SiO_2 vs. CaO trend for plagioclase hosted SMIs and the SiO_2 vs. Al_2O_3 for alkali feldspar hosted SMIs. Accuracy of the quantification of the SMIs by LA-ICP-MS is between 10 and 30 % for most elements (Chang and Audétat, 2021).

For the sulfide melt inclusions the laser was operated at 5 Hz and an energy density 5-10 J/cm2 on the sample surface, the analyzed isotopes include ^{25}Mg, ^{27}Al, ^{30}Si, ^{32}S, ^{43}Ca, ^{49}Ti, ^{55}Mn, ^{57}Fe, ^{59}Co, ^{62}Ni, ^{65}Cu, ^{66}Zn, ^{75}As, ^{82}Se, ^{98}Mo, ^{109}Ag, ^{105}Pd, ^{109}Ag, ^{125}Te, ^{195}Pt, ^{208}Pb and ^{209}Bi. A dwell time of 10 ms was used for all elements excepted for Pd (20 ms), Pt (30 ms) and Au (30 ms). In the case of the sulfide inclusions, host was numerically subtracting until no MgO was left. External standardization for Fe and S was based on a crystal of pyrrhotite previously characterized by EPMA and showing constant Fe (60.28 wt.%, 1σ = 0.20 %, n= 40) and S (40.16 wt.%, 1σ = 0.14 %, n= 40) contents. The NIST SRM 610 was used as external standard for all other elements. Internal standardization was performed by normalizing the sum of S, Fe, Co, Ni and Cu to 100 wt%. The accuracy of this method was evaluated by Zhang & Audétat (2017; Electronic Appendix Table S1) on different sulfide minerals, and the values they obtained for Cu, Fe, Te, Sb, and S were in agreement within 3% with the reference/theoretical values, and within 7% for the other elements (Ni, Se, and Pb). Chang & Audétat (2018) report that the ^{105}Pd signal is affected by a polyatomic interference with the ^{65}Cu^{40}Ar, and they show that this interference follows a simple linear equation ^{105}Pd (ppm) = 0.4063*Cu (wt%)-1.2711; R^2 = 0.9949). Therefore, the contribution of the ^{65}Cu^{40}Ar to the obtained ^{105}Pd concentrations was numerically subtracted according to this equation. Uncertainties associated with the LA-ICP-MS analyses of sulfide inclusions are ≤ 5-8 % (Zhang and Audétat, 2017a; Chang and Audétat, 2018).

Micro-XRF

Section elemental mapping was performed with a Bruker M4 TORNADO μXRF spectrometer at Université Laval, Québec (Canada). Analytical conditions were set to a voltage of 50 kV and a current of 300 μA, with a beam size of 20 μm, an acquisition time of two milliseconds per pixel and a step size of 20 μm.

Oxythermobarometry

Oxybarometers

To determine the oxygen fugacity of the investigated rocks, we used two different oxybarometers: (i) the Fe–Ti oxide pairs (Ghiorso & Evans 2008), and (ii) the partitioning of vanadium between olivine and melt (Shishkina et al., 2018).

Ilmenite-magnetite

The analyzed oxides were generally devoid of exsolution, and the selected ilmenite and magnetite grains were either intergrown or touching each other. All selected Fe-Ti oxide pairs were then tested for equilibrium using the method of Bacon & Hirschmann (1988). Pairs that did not pass this test were not considered further. The Fe-Ti oxide pairs that passed the equilibrium test were then used to calculate fO_2 and temperature with the model of Ghiorso & Evans (2008). Ilmenite and magnetite pairs were found in the basanite (BR-03, n=7 and BR-07, n=17) in the basaltic trachyandesite (BR-08, n=6) and in the trachyandesite (BR-06, n=26). For samples BR-03, BR-07 and BR-06 the ilmenite-magnetite oxybarometer gives values between ΔFMQ -1 ± 0.4 and -1.8 ± 0.1 and low temperatures between 860ºC and 700ºC. Such low temperature must indicate that the ilmenite-magnetite pairs were reequilibrated during the cooling of the extrusive rocks and that they record the oxygen fugacity of the melt having probably already been degassed (Hou et al., 2020). Therefore, the values obtained for these samples were discarded. However, the ilmenite-magnetite pairs of sample BR-08 record high-temperature 1110 ± 80ºC and higher oxygen fugacity ΔFMQ 0.4 ± 0.3 and are considered to be representative of the temperature and oxygen fugacity of the primitive magma. In table 1 we report the average value and the calculated 1σ standard deviation. Ghiorso & Evans (2008) did not specify any uncertainty for the calculated fO2 values, but Arató and Audétat (2017) estimated them at ±0.5 log units.

partitioning of vanadium between olivine and melt

The partitioning of vanadium between olivine and melt (Shishkina et al., 2018) were used for the three samples of basanites (BR-03, n=9; BR-07, n=4; BR-11 n=4) and for two samples of trachybasalts (BR-04 n= 1; BR-10, n=4). Oxygen fugacity was calculated using the V concentration of olivine-hosted silicate melt inclusions and the V concentration of the host olivine. The values reported in Table 1 correspond to the average fO_2 value and the corresponding 1σ standard deviation. Calculated 2σ uncertainty of the calculation method using the equation provided by Shishkina et al. (2018) are between 0.8 and 0.9 log units.

Thermometers

Olivine-spinel thermometer

The Al-in-olivine thermometer based on partition coefficient of aluminum between olivine and Cr-rich spinel was used with the composition of olivine-hosted Cr-rich spinel inclusions and the composition of olivine directly next to the inclusions. Both were determined by EPMA (see above). The temperatures were calculated using the equation 6 published by Coogan et al. (2014). Temperatures were calculated for two samples of basanites (BR-03, n=9; BR-07, n=8), two samples of trachybasalts (BR-09 n=2; BR-10 n=5) and one sample of trachyandesite (BR-06 n=6). The temperatures reported in Table 1 correspond to the average temperature obtained and the corresponding 1σ standard deviation.

Clinopyroxene-liquid thermometer

For the orthopyroxene-liquid thermobarometer we followed the approach described by Neave et al. (2019). We used the clinopyroxene compositions determined by EPMA. For the liquid composition, we follow the method described by Neave and Putirka (2017), each clinopyroxene was iteratively matched to the regional whole rock composition compiled from this study and the literature (Besson, 1978; Chauvel and Jahn 1980, Gourgaud et al., 1980; Briot et al., 1991; Sorensen et al., 1999). A matched was considered satisfactory when the composition of clinopyroxene and the liquid passed the four different equilibrium filter: (1) $KD^{Mg-Fe}_{cpx-liq}$ values were within 0.03 of equilibrium values calculated assuming a melt $Fe^{3+}/\sum Fe$ value of 0.15 (Putirka, 2008); and (2) Diopside-Hedenbergite (DiHd), Enstatite-Ferrosilite (EnFs), and Calcium-Tschermak (CaTs) component contents were within 1SEE of predicted values (Putirka, 1999; Mollo et al., 2013). From matched clinopyroxene and the liquid compositions, the temperature of crystallization of the clinopyroxene was determined using the equation 33 from Putirka (2008). The number of matched clinopyroxene and the liquid composition pairs for the different samples are BR-03 n=31, BR-04 n=50, BR-06 n=35, BR-07 n=24, BR-08 n=44, BR-09 n=19; BR-10 n=12; BR-11 n=62 and BR-12 n=22. The temperatures reported in Table 1 correspond to the average temperature obtained and the corresponding 1σ standard deviation.

Amphibole thermometer

Crystallization temperatures were determined based on equation 5 of Purtika (2016) using only the composition of amphibole determined by EPMA. This equation is independent of the liquid composition, and the uncertainty inherent to this calculation has been stated at ± 30ºC. A total of 50 temperatures were calculated for sample BR-08 and 5 for sample BR-06. The temperatures reported in Table 1 correspond to the average temperature obtained and the corresponding 1σ standard deviation.

Two-feldspar thermometer

Crystallization temperatures were calculated using the rim compositions of touching pairs of plagioclase and alkali-feldspar determined by EPMA. Temperatures were calculated using the equation 27b of Purtika (2008) using a pressure fixed at 4 kbar. The uncertainty inherent to this calculation has been stated at ± 30ºC. A total of 4 temperatures were calculated for sample BR-08 and 6 for BR-06. The temperatures reported in Table 1 correspond to the average temperature obtained and the corresponding 1σ standard deviation.

Barometers

Pressures were calculated from clinopyroxene composition determined by EMPA using machine learning approach described by Petrelli et al. (2020) based on random forest analyses. Calculations were performed using the Python scripts provide by Petrelli et al. (2020). Pressures were calculated from a large number of pyroxenes for each sample: BR-03 n=38, BR-04 n=58, BR-06 n=54, BR-07 n=25, BR-08 n=48, BR-09 n=30; BR-10 n=30, BR-11 n= 117, and BR-12 n=30. The pressures reported in Table 1 correspond to the average pressure obtained and the corresponding 1σ standard deviation.

Quantitative sulfide fractionation model.

A quantitative model similar to those described in Rottier et al. (2019) was developed to constrain the Cu and Au contents of residual melt during the evolution of the magmatic system.

The model was constructed as follows:

(1) The chemical evolution of the magma was parametrized by using the trends defined by the whole rock data and compositions of rock matrices.

(2) Magma crystallinity was linked to SiO_2 by monitoring the enrichment in Rb as a function of SiO_2 observed in the whole rock compiled from this study and literature (Besson, 1978; Chauvel and Jahn 1980, Gourgaud et al., 1980; Briot et al., 1991; Sorensen et al., 1999). For this purpose, we assumed that Rb behaved 100% incompatible during magma differentiation, which is reasonable considering the very low Rb content of the rock-forming minerals.

(3) Temperature evolution was set to follow the temperature decrease from 1140ºC to 840ºC obtained with the different thermometers.

(4) As no anhydrite was observed neither as inclusions in the phenocrysts or in the matrix of different rocks, we only model the S^{2-} concentration in the evolved melt composition. The sulfur solubility of the melt was calculated from (i) the NFM model of Fortin et al. (2015) as modified by D'Souza and Canil (2018) that take in consideration the positive effect of Na and K contents of the silicate melt on the SCSS and (ii) from the evolving composition of the modeled silicate melt. Sulfur content above the calculated SCSS was considered to be fully precipitated as sulfide (either 100% MSS or 100% SL). The starting sulfur concentration was fixed at 1200 ppm to reach sulfide saturation when the TiO_2 reach ~3.5 wt.% based on the Cu concentration drop observed in the silicate melt inclusions (Fig. 2B). Considering the oxygen fugacity of the magmas (ΔFMQ between 0.4 and 2.3), the pressure of magma differentiation (between 4 and 6 kbar), and the experimental work of Matjuschkin et al. (2016) and Jégo et al. (2016) part of the sulfur dissolved in the silicate melt can be present as S^{6+}. In such case, the sulfur solubility of the melt will be higher, but the proportion of sulfide formed when sulfur saturation is reached during magma differentiation will be similar that in a system where S is only present as S^{2-}. Nonetheless, the initial concentration of sulfur will need to be higher to reach sulfur and sulfate saturation. As sulfate precipitation will not affect the Cu and Au content of the residual melt and that we have no constraint on the initial sulfur content of the silicate melt, ignoring the potential occurrence of S^{6+} in the silicate melt will not affect the result of the model as volume of precipitated sulfide.

(5) The $D^{MSS/SM}_{Au}$ is calculated using the equation from Li et al. (2019) and the sulfur concentration at sulfide saturation (SCSS) values calculated from the NFM model of Fortin et al. (2015) as modified by D'Souza and Canil (2018). Calculated $D^{MSS/SM}_{Au}$ are between ~ 30 and ~1300 and they increase with magma differentiation. Such values are coherent with the $D^{MSS/SM}_{Au}$ values experimentally determined by Li and Audétat (2012) and (2013) from MS-saturated basanite melt. For SL, the $D^{SL/SM}_{Au}$ was fixed at 10000 consistent with experimental values (Li et al., 2019, 2021). The $D^{MSS/SM}_{Cu}$, $D^{SL/SM}_{Cu}$, $D^{MSS/SM}_{Ni}$ and $D^{SL/SM}_{Ni}$ were calculated using the equations given in Li and Audétat (2015) and Li et al. (2021). The partition coefficients of the Cu and Au between other minerals and silicate melts were set to zero. Since Ni also partitions strongly into silicate minerals (e.g., olivine, pyroxene and amphibole), the partition coefficient and the starting melt content of Ni were adjusted to match the modeled range of other metals in sulfide within the range of 0.01–3 wt% Ni, please see Chang and Audétat (2021) for more details.

(6) The initial Cu and Au concentration of the melt were fixed at 100 ppm and 15 ppb, respectively.

(7) Three different models were constructed (i) one assuming pure equilibrium, (ii) two assuming that at each modeled crystallization step 50% or 100% of the formed sulfide are fractionated out of the system.

Additional references:

Bacon, C. R., & Hirschmann, M. M. (1988). Mg/Mn partitioning as a test for equilibrium between coexisting Fe-Ti oxides. American Mineralogist, 73, 57-61.

Besson, J.C. (1978) - Les formations volcaniques du versant oriental du massif du Mont-Dore (Massif Central français), feuille 1/25 000 Veyre-Monton 5-6, Thèse de Illème cycle, Clermont Fd., 167 p.

Briot, D., Cantagrel, J. M., Dupuy, C., Harmon, R. S. (1991). Geochemical evolution in crustal magma reservoirs: Trace-element and Sr, Nd, O isotopic variations in two continental intraplate series at Monts Dore, Massif Central, France. Chemical Geology, 89, 281-303.

Brousse R., Tempier P. (1981) Carte geol. France (1/50 000),feuille BOURG-LASTIC (716) – Orléans : Bureau de recherches géologiques et minières.

Chauvel, C., & Jahn, B. M. (1984). Nd and Sr isotope and REE geochemistry of alkali basalts from the Massif Central, France. Geochimica et Cosmochimica Acta, *48*, 93-110.

Coogan, L. A., Saunders, A. D., & Wilson, R. N. (2014). Aluminum-in-olivine thermometry of primitive basalts: Evidence of an anomalously hot mantle source for large igneous provinces. Chemical Geology, 368, 1-10.

Ghiorso, M. S., Evans, B. W. (2008). Thermodynamics of rhombohedral oxide solid solutions and a revision of the Fe-Ti two-oxide geothermometer and oxygen-barometer. American Journal of science, 308, 957-1039.

Gourgaud, A., Bourdier, J.L., Vincent, P.M., (1980) Mélange de magmas sur-saturés et sous-saturés dans le volcan du Sancy (Monts Dore, Massif Central Francais. Compte Rendu de l'Académie des Sciences de Paris, 291, 175-178.

Halter, W. E., Pettke, T., & Heinrich, C. A. (2004). Laser-ablation ICP-MS analysis of silicate and sulfide melt inclusions in an andesitic complex I: analytical approach and data evaluation. Contributions to Mineralogy and Petrology, 147, 385-396.

Hou, T., Botcharnikov, R., Moulas, E., Just, T., Berndt, J., Koepke, J., ... & Holtz, F. (2020). Kinetics of Fe–Ti oxide re-equilibration in magmatic systems: implications for thermo-oxybarometry. Journal of Petrology, 61, egaa116.

Mollo, S., Putirka, K., Misiti, V., Soligo, M., & Scarlato, P. (2013). A new test for equilibrium based on clinopyroxene–melt pairs: clues on the solidification temperatures of Etnean alkaline melts at post-eruptive conditions. Chemical Geology, 352, 92-100.

Neave, D. A., Bali, E., Guðfinnsson, G. H., Halldórsson, S. A., Kahl, M., Schmidt, A. S., Holtz, F. (2019). Clinopyroxene–liquid equilibria and geothermobarometry in natural and experimental tholeiites: the 2014–2015 Holuhraun eruption, Iceland. Journal of Petrology, 60, 1653-1680.

Pettke, T. (2006). In situ laser-ablation ICPMS analysis of melt inclusions and prospects for constraining subduction zone magmatism. Melt Inclusions in Plutonic Rocks. Contributions to Mineralogy and Petrology (eds Webster JD), 36, 51-80.

Putirka, K. (2016). Amphibole thermometers and barometers for igneous systems and some implications for eruption mechanisms of felsic magmas at arc volcanoes. American Mineralogist, 101, 841-858.

Putirka, K. (1999). Clinopyroxene+ liquid equilibria to 100 kbar and 2450 K. Contributions to Mineralogy and Petrology, 135, 151-163.

Sorensen H., Bernth U., Brousse R. (1999) Trachytes and phonolites from the Mont-Dore region, Auvergne, France. Geolines, 9, 114-118.

Supplementary Table 1 – composition of the silicate melt inclusions

			Major element Wt.%									Trace elements (ppm)																	
Rock type	Sample #	Host mineral	Na_2O	MgO	Al_2O_3	SiO_2	K_2O	CaO	TiO_2	MnO	FeO_t	Li	Zn	As	Rb	Sr	Ag	Ba	Pb	Y	P	V	Ni	Cu	Zr	Nb	Cs	Th	U
Basnite	BR-03	Ol	2.5	12.9	11.9	38.6	1.1	11.2	2.8	0.3	18.7	(20)	247	(11)	24	576	(3)	353	2	21	1191	314	657	178	187	45	(0)	3	1
Basnite	BR-03	Ol	3.0	13.6	13.6	37.9	1.4	12.0	3.3	0.2	15.0	12	211	(5)	28	656	0	411	5	24	1482	399	117	97	206	51	0	3	1
Basnite	BR-03	Ol	2.6	10.8	15.9	40.4	2.0	15.4	3.7	0.1	9.2	(15)	93	(12)	39	799	1	353	7	30	1455	443	549	168	246	50	(1)	3	1
Basnite	BR-03	Ol	2.8	12.5	15.1	38.9	0.9	16.8	4.0	0.1	9.0	(11)	31	0	16	534	0	351	12	32	1091	450	843	137	263	51	(1)	3	1
Basnite	BR-03	Ol	3.0	15.1	14.7	36.8	1.4	13.7	3.4	0.1	11.7	(22)	147	0	26	660	1	422	2	27	871	447	1054	124	218	56	(1)	4	(0)
Basnite	BR-03	Ol	2.7	7.9	14.4	43.5	1.6	17.3	3.6	0.1	8.8	8	53	(4)	33	656	0	439	2	30	1550	396	129	110	248	47	0	3	1
Basnite	BR-03	Al-, Ti-rich Cpx	1.3	15.0	13.4	44.6	0.6	10.4	3.9	0.1	10.6	36	79	1	10	387	(2)	183	4	26	841	477	80	45	172	27	(0)	1	0
Basnite	BR-03	Al-, Ti-rich Cpx	1.8	7.9	14.1	43.5	0.8	13.4	5.4	0.4	12.8	69	107	2	23	522	(1)	155	3	59	762	75	0	40	428	27	(0)	2	1
Trachybasalt	BR-04	Ol	5.2	0.0	18.8	58.3	3.5	8.2	3.0	0.0	3.0	(55)	(153)	(50)	81	897	(13)	1076	9	44	3666	245	(47)	74	460	128	(3)	13	5
Trachybasalt	BR-04	Al-, Ti-rich Cpx	5.7	9.3	18.1	42.0	3.3	14.2	1.6	0.3	5.6	(17)	98	(16)	70	746	(3)	749	7	55	2668	0	48	65	724	103	1	12	3
Trachybasalt	BR-04	Al-, Ti-rich Cpx	3.8	7.6	15.4	43.9	2.4	14.8	3.5	0.2	8.4	(10)	87	0	53	506	(2)	566	6	41	2022	366	13	62	418	83	1	9	2
Trachybasalt	BR-04	Al-, Ti-rich Cpx	4.3	6.4	15.3	45.4	3.0	14.8	2.9	0.2	7.7	(19)	118	(15)	62	546	(5)	612	6	26	2418	346	0	75	363	90	1	11	3
Trachybasalt	BR-04	Al-, Ti-rich Cpx	6.8	6.2	17.8	45.7	4.4	11.8	2.5	0.2	4.5	0	(80)	0	94	694	2	948	7	17	3119	0	0	103	396	115	(2)	15	5
Trachybasalt	BR-04	Al-, Ti-rich Cpx	4.4	7.8	16.0	43.7	2.8	15.7	3.1	0.2	6.3	0	(40)	0	67	513	(4)	639	5	38	2179	220	0	54	389	80	2	11	3
Trachybasalt	BR-04	Al-, Ti-rich Cpx	4.0	8.5	14.7	42.8	2.4	15.7	2.9	0.2	8.7	(12)	84	(10)	55	508	(3)	623	7	46	2292	315	0	62	444	89	1	10	3
Trachybasalt	BR-04	Al-, Ti-rich Cpx	4.5	7.7	16.5	43.7	2.7	11.9	4.0	0.2	8.8	(24)	104	0	54	614	1	668	6	47	2190	376	0	60	534	108	1	11	3
Trachybasalt	BR-04	Al-, Ti-rich Cpx	3.6	7.9	13.8	43.5	2.5	14.6	3.4	0.2	10.4	(11)	113	(7)	60	515	(2)	580	7	41	2246	477	53	61	404	69	1	9	2
Trachybasalt	BR-04	Al-, Ti-rich Cpx	4.1	7.8	16.7	43.6	2.2	12.6	4.1	0.2	8.7	(12)	99	(9)	52	492	0	557	6	47	1986	461	16	45	460	74	1	9	2
Trachybasalt	BR-04	Al-, Ti-rich Cpx	4.8	7.0	15.4	44.6	3.1	14.1	3.1	0.2	7.7	(9)	115	(8)	75	588	(2)	699	8	37	2867	256	14	58	440	95	1	11	4
Trachybasalt	BR-04	Al-, Ti-rich Cpx	4.3	8.0	15.4	43.3	2.4	13.7	3.7	0.2	9.0	0	83	(9)	58	532	0	609	5	40	2203	403	0	57	414	86	1	11	3
Trachybasalt	BR-04	Al-, Ti-rich Cpx	4.0	9.1	15.0	42.1	2.3	13.6	4.7	0.2	9.0	(44)	(91)	(28)	55	464	(9)	528	6	31	2113	732	0	51	380	84	(2)	9	3
Trachyandesite	BR-06	Pl	5.0	0.3	23.0	59.2	6.1	3.0	0.8	0.1	2.5	(22)	87	(23)	120	1965	(4)	1255	14	22	373	54	0	(8)	778	131	3	21	7
Trachyandesite	BR-06	Na-, Si-rich Cpx	7.9	1.7	19.1	55.5	6.1	4.8	0.5	0.2	4.1	49	127	7	228	140	0	198	23	25	1310	47	0	18	1071	102	4	26	9
Trachyandesite	BR-06	Na-, Si-rich Cpx	6.8	3.8	20.4	49.8	5.1	10.2	0.9	0.3	2.7	394	153	(15)	171	359	(5)	486	15	35	490	140	0	34	1264	94	4	25	8
Trachyandesite	BR-06	Pl	3.8	0.6	19.7	68.3	3.2	1.0	0.7	0.1	2.5	(9)	65	0	96	882	(2)	1157	8	31	969	54	(11)	40	358	80	3	10	3
Basanite	BR-07	Al-, Ti-rich Cpx	3.5	9.9	12.0	49.6	1.9	10.0	1.6	0.4	11.1	21	134	(1)	42	1167	(0)	733	8	62	3591	120	4	113	368	103	0	9	2
Basanite	BR-07	Al-, Ti-rich Cpx	7.6	0.3	14.9	68.4	4.0	0.0	0.0	0.7	4.1	0	68	(6)	110	1172	(1)	957	11	76	1133	0	0	19	52	176	2	16	5
Basaltic trachyandesite	BR-08	Afs	3.7	0.3	18.7	60.2	13.8	0.5	0.5	0.1	2.2	21	59	(6)	319	413	(1)	1460	0	11	(79)	23	(8)	8	802	111	4	31	11
Basaltic trachyandesite	BR-08	Afs	4.2	0.5	18.7	59.4	12.6	1.2	0.5	0.1	2.8	26	85	5	298	245	(1)	1273	191	19	70	32	(6)	17	820	131	3	37	12
Trachybasalt	BR-09	Al-, Ti-rich Cpx	2.8	7.5	14.0	44.0	1.6	15.2	2.8	0.2	11.9	(25)	128	(26)	38	447	(5)	407	5	46	559	463	(30)	44	235	27	(2)	6	1
Trachybasalt	BR-09	Al-, Ti-rich Cpx	2.5	5.1	17.1	47.4	1.2	11.9	3.6	0.2	10.9	29	96	0	28	741	1	459	4	69	2330	454	0	84	301	66	(1)	6	1
Trachybasalt	BR-09	Al-, Ti-rich Cpx	2.5	2.3	16.2	53.7	0.9	9.0	3.5	0.2	11.8	19	(53)	(14)	19	554	(4)	167	2	51	1151	337	52	0	318	32	(1)	5	1
Trachybasalt	BR-09	Al-, Ti-rich Cpx	4.7	10.7	16.4	40.6	2.6	12.0	2.9	0.2	9.9	31	113	0	62	1077	(1)	781	6	26	2819	354	(13)	87	324	106	1	13	4

Red values in brackets are the limit of detections.

Supplementary Table 1 – continuation

			Major element Wt.%									Trace elements (ppm)																	
Rock type	Sample #	Host mineral	Na_2O	MgO	Al_2O_3	SiO_2	K_2O	CaO	TiO_2	MnO	FeO_t	Li	Zn	As	Rb	Sr	Ag	Ba	Pb	Y	P	V	Ni	Cu	Zr	Nb	Cs	Th	U
Trachybasalt	BR-10	Al-, Ti-rich Cpx	3.3	5.6	15.5	58.4	2.0	3.2	3.6	0.1	8.2	41	(34)	(9)	56	788	(2)	541	6	61	1376	22	90	81	702	77	(1)	10	3
Trachybasalt	BR-10	Na-, Si-rich Cpx	4.7	6.6	16.2	53.1	3.0	5.5	1.9	0.2	8.9	51	62	(5)	74	691	0	684	5	30	1075	200	87	123	278	101	1	13	4
Trachybasalt	BR-10	Al-, Ti-rich Cpx	4.8	4.8	17.7	47.9	3.7	14.3	1.8	0.2	4.7	40	130	(3)	140	596	0	1259	12	70	452	150	0	35	747	92	3	5	2
Trachybasalt	BR-10	Al-, Ti-rich Cpx	5.0	0.0	13.6	70.7	3.2	2.7	0.0	0.2	4.7	(40)	(141)	(30)	93	1068	(9)	1011	12	32	2679	0	0	48	574	133	(3)	16	5
Trachybasalt	BR-10	Al-, Ti-rich Cpx	10.4	2.5	15.1	52.9	9.3	4.5	0.0	1.4	3.9	33	332	(14)	199	1178	(2)	1899	17	76	1345	0	0	51	995	216	3	28	6
Trachybasalt	BR-10	Al-, Ti-rich Cpx	6.0	4.3	19.1	48.9	3.5	9.2	2.0	0.1	7.0	25	(35)	0	83	1412	0	1045	9	21	2533	213	127	109	348	143	1	13	4
Trachybasalt	BR-10	Al-, Ti-rich Cpx	4.4	6.8	17.4	44.9	2.9	13.1	2.6	0.2	7.7	26	79	(5)	78	1236	(1)	1013	8	32	1945	230	35	57	500	129	1	12	4
Basanite	BR-11	Ol	0.4	3.5	14.6	50.5	0.4	14.1	3.2	0.1	13.2	(9)	105	(10)	237	688	(2)	571	4	26	1232	371	1777	183	318	72	(1)	7	1
Basanite	BR-11	Ol	0.6	7.1	17.6	44.5	0.6	18.2	4.0	0.1	7.3	2	60	(3)	200	1230	0	667	9	34	2469	432	390	136	356	91	0	7	2
Basanite	BR-11	Ol	0.5	4.3	16.2	48.8	0.4	16.2	3.6	0.1	9.9	(2)	137	2	330	694	(0)	522	9	29	1895	474	413	141	315	70	0	6	1
Basanite	BR-11	Ol	0.5	6.2	16.3	45.8	0.5	15.5	4.0	0.1	11.2	(13)	200	0	293	1181	0	682	6	35	3270	452	965	103	414	105	(1)	10	2
Basanite	BR-11	Al-, Ti-rich Cpx	3.8	10.2	17.5	41.0	2.1	13.4	3.3	0.2	8.6	45	(33)	(10)	45	927	(2)	777	7	40	2536	281	51	63	485	92	1	9	3
Basanite	BR-11	Al-, Ti-rich Cpx	3.6	10.0	16.5	41.2	1.9	11.3	4.1	0.2	11.1	7	101	(1)	37	1056	0	637	7	35	2780	419	72	70	374	94	0	8	2
Basanite	BR-11	Al-, Ti-rich Cpx	2.8	7.5	13.8	44.0	1.4	15.9	3.8	0.2	10.8	39	92	(1)	26	819	0	518	3	35	1738	416	0	55	252	68	0	5	1
Basanite	BR-11	Al-, Ti-rich Cpx	4.1	6.8	14.7	49.1	2.2	7.6	2.9	0.3	12.4	38	132	(5)	51	1238	0	1021	6	36	3189	342	81	104	426	118	1	10	2
Basanite	BR-11	Na-, Si-rich Cpx	4.8	3.0	17.2	51.5	3.0	10.4	2.2	0.3	7.6	31	128	(8)	108	385	(3)	583	12	50	463	188	0	89	643	56	2	16	4
Basanite	BR-11	Al-, Ti-rich Cpx	5.4	6.0	18.5	46.1	3.0	3.0	3.5	0.3	14.2	33	168	(3)	65	1551	0	1018	4	30	4533	424	77	111	485	152	1	12	3
Basanite	BR-11	Al-, Ti-rich Cpx	3.0	4.8	19.3	47.9	1.8	10.0	4.8	0.1	8.3	2	77	(3)	27	908	0	565	1	38	1605	322	6	177	254	64	0	4	1
Basanite	BR-11	Al-, Ti-rich Cpx	2.8	7.8	13.6	43.7	2.1	12.2	4.1	0.2	13.6	23	146	1	95	552	0	286	6	25	1349	446	65	148	322	91	1	7	2
Basanite	BR-11	Al-, Ti-rich Cpx	0.4	14.4	15.2	37.3	0.3	14.6	3.2	0.2	14.4	6	221	(4)	394	822	(1)	550	18	32	2021	377	0	165	343	84	1	6	1
Basanite	BR-12	Ol	5.9	9.4	17.2	41.8	4.1	12.0	2.2	0.2	7.3	0	197	(5)	96	1075	0	1055	10	57	13994	146	0	59	434	150	1	17	4
Basanite	BR-12	Al-, Ti-rich Cpx	4.2	7.5	17.3	44.0	2.9	13.7	2.9	0.2	7.3	7	96	(7)	61	795	(1)	822	10	43	1756	236	66	70	552	114	1	11	3
Basanite	BR-12	Al-, Ti-rich Cpx	3.0	8.2	15.7	43.1	2.0	14.4	4.0	0.2	9.3	(4)	92	(3)	52	676	0	563	7	62	1791	373	0	49	708	84	1	9	2
Basanite	BR-12	Al-, Ti-rich Cpx	2.7	8.2	16.4	43.2	1.5	12.6	4.9	0.3	10.2	(5)	102	(5)	35	657	(1)	513	5	74	1305	467	0	38	812	77	1	8	2
Basanite	BR-12	Al-, Ti-rich Cpx	5.1	7.0	17.7	44.6	2.9	10.4	3.0	0.2	9.0	11	80	(7)	66	938	0	891	9	18	2058	360	75	323	343	122	1	10	3

Red values in brackets are the limit of detections.

Supplementary Table 2 – composition of the sulfide melt inclusions

			Major element (wt.%)					Trace element (ppm)												
Rock type	Sample #	Host mineral	S	Fe	Co	Ni	Cu	Mn	Zn	As	Se	Mo	Pd	Pd corrected	Ag	Te	Pt	Au	Pb	Bi
Basanite	BR-03	Al-, Ti-rich Cpx	52	47	0.12	0.18	0.89	3132	160	(49)	(239)	(50)	(44.9)	(44.9)	(12.3)	(22.0)	(3.8)	(2.7)	(3)	(1.1)
Basanite	BR-03	Al-, Ti-rich Cpx	31	68	0.13	0.23	0.58	1013	(134)	(69)	(295)	(73)	12.7	13.7	(27.9)	(81.0)	(5.6)	2.1	78	(1.8)
Basanite	BR-03	Al-, Ti-rich Cpx	45	55	0.13	0.09	0.41	(59)	(164)	(97)	(633)	(102)	16.3	17.4	8.7	(92.1)	(9.7)	0.2	8	(2.8)
Basanite	BR-03	Al-, Ti-rich Cpx	54	45	0.12	0.21	1.16	(97)	347	(176)	(865)	(139)	198.2	199.0	(70.1)	(179.9)	8.3	1.8	52	(4.5)
Basanite	BR-03	Al-, Ti-rich Cpx	36	62	0.15	0.51	1.19	303	(152)	(121)	(469)	(80)	(183.9)	(183.9)	2.3	(136.4)	(11.7)	(5.7)	(7)	(2.9)
Basanite	BR-03	Al-, Ti-rich Cpx	37	59	0.20	1.41	2.45	1427	136	(51)	(206)	(30)	22.1	22.4	1.3	(38.3)	(3.7)	(2.7)	10	(1.2)
Basanite	BR-03	Al-, Ti-rich Cpx	50	49	0.14	0.41	0.58	1468	(99)	51	(158)	55	20.1	21.1	1.3	(40.7)	(2.4)	(2.0)	52	(0.9)
Basanite	BR-03	Al-, Ti-rich Cpx	57	41	0.11	0.61	0.80	2028	306	(76)	(443)	(80)	(91.1)	(91.1)	(30.6)	(95.5)	(8.3)	2.7	(7)	(2.4)
Basanite	BR-03	Al-, Ti-rich Cpx	42	56	0.16	0.67	1.14	588	239	(103)	(345)	(96)	(98.6)	(98.6)	(30.5)	(112.3)	(8.1)	1.6	(6)	(2.0)
Basanite	BR-03	Al-, Ti-rich Cpx	59	40	0.11	0.73	0.30	534	(353)	(126)	(738)	(141)	12.9	14.1	16.6	(136.2)	0.3	1.1	46	(4.0)
Basanite	BR-03	Al-, Ti-rich Cpx	47	50	0.17	1.40	1.82	(44)	(188)	(71)	(376)	(49)	(128.2)	(128.2)	6.8	(74.2)	(5.7)	(6.4)	(6)	(2.2)
Basanite	BR-03	Al-, Ti-rich Cpx	58	39	0.12	1.16	1.83	(150)	601	(267)	(1503)	(351)	(365.1)	(365.1)	(113.2)	(349.8)	2.0	(23.6)	(20)	(6.4)
Basanite	BR-07	Al-, Ti-rich Cpx	49	38	0.14	1.48	11.24	(85)	1111	(218)	(1494)	(79)	(36.2)	(36.2)	0.0	(308.3)	3.3	(14.6)	219	(5.7)
Basanite	BR-07	Al-, Ti-rich Cpx	34	59	0.09	0.64	5.87	4448	(1121)	(361)	(2487)	(135)	(62.3)	(62.3)	(91.8)	(496.7)	(16.4)	3.0	56	(9.6)
Basanite	BR-07	Al-, Ti-rich Cpx	37	63	0.05	0.05	0.24	1111	252	(8)	(54)	(6)	(2.5)	(2.5)	3.1	(10.2)	(0.5)	0.2	3	0.3
Basanite	BR-07	Al-, Ti-rich Cpx	32	54	0.09	0.88	13.42	1460	1343	(127)	(768)	(32)	(25.5)	(25.5)	81.9	(205.5)	(6.3)	(7.4)	318	(3.7)
Basanite	BR-07	Al-, Ti-rich Cpx	33	62	0.15	0.26	4.76	7563	1048	(471)	(1845)	(261)	(96.6)	(96.6)	72.4	(375.3)	(21.1)	(21.9)	100	(11.0)
Basanite	BR-07	Al-, Ti-rich Cpx	40	54	0.20	0.40	6.06	1849	520	(291)	(1148)	(167)	(62.2)	(62.2)	(37.9)	(227.1)	(13.3)	(13.5)	76	(6.9)
Basanite	BR-07	Al-, Ti-rich Cpx	38	61	0.16	0.17	1.45	674	145	(75)	(385)	(33)	(17.1)	(17.1)	(12.9)	(58.6)	(3.1)	(3.6)	(5)	(1.3)
Basanite	BR-07	Al-, Ti-rich Cpx	37	60	0.16	0.19	2.27	83	144	(39)	198	(20)	(12.8)	(12.8)	(5.6)	(47.2)	(2.3)	(2.9)	8	(1.2)
Basanite	BR-07	Al-, Ti-rich Cpx	35	62	0.14	0.19	2.30	1456	167	(105)	(319)	(40)	(19.5)	(19.5)	(8.4)	(51.3)	(4.7)	(4.6)	42	(1.7)
Basaltic trachyandesite	BR-08	Al-, Ti-rich Cpx	44	55	0.06	0.08	0.25	1056	(199)	(96)	(456)	(67)	(28.3)	(28.3)	(22.0)	(149.7)	(7.4)	0.2	(7)	(2.9)
Basaltic trachyandesite	BR-08	Al-, Ti-rich Cpx	36	63	0.12	0.30	0.52	162	(143)	(79)	(398)	(41)	(28.4)	(28.4)	(24.9)	(107.9)	(5.6)	(5.1)	14	(2.7)
Basaltic trachyandesite	BR-08	Al-, Ti-rich Cpx	38	57	0.26	2.58	2.74	(195)	(617)	(544)	(1887)	(257)	(188.1)	(188.1)	(88.0)	(572.8)	7.5	(19.4)	(28)	(12.0)
Basaltic trachyandesite	BR-08	Al-, Ti-rich Cpx	48	50	0.24	1.00	1.31	745	(378)	(236)	(963)	(98)	(75.2)	(75.2)	(44.0)	(391.2)	(8.7)	(10.4)	(12)	(5.7)
Basaltic trachyandesite	BR-08	Al-, Ti-rich Cpx	40	59	0.14	0.50	0.27	1692	(279)	418	(697)	(90)	(51.9)	(51.9)	19.1	(211.9)	(7.6)	(6.0)	266	(4.3)
Trachybasalt	BR-08	Al-, Ti-rich Cpx	37	59	0.14	0.23	3.90	1367	505	(52)	(178)	(23)	(19.3)	(19.3)	10.8	(43.1)	(3.5)	0.5	11	(2.0)
Trachybasalt	BR-10	Al-, Ti-rich Cpx	35	60	0.18	1.27	3.26	1091	140	(24)	(135)	(17)	5.6	5.6	2.3	(20.3)	(1.5)	(1.7)	6	(1.0)
Trachybasalt	BR-10	Al-, Ti-rich Cpx	32	66	0.13	0.45	0.79	1522	268	(50)	(230)	(28)	(21.8)	(21.8)	0.0	(33.4)	(3.9)	(2.2)	(5)	(1.5)
Trachybasalt	BR-10	Al-, Ti-rich Cpx	37	61	0.14	0.11	2.01	2198	936	(76)	(345)	(59)	16.9	17.3	5.4	(81.8)	(4.8)	0.7	(7)	(3.3)
Trachybasalt	BR-10	Al-, Ti-rich Cpx	59	38	0.13	0.69	1.96	3625	(236)	(88)	(350)	(87)	(31.1)	(31.1)	(34.6)	(125.8)	(5.2)	3.1	(7)	(3.5)

Red values in brackets are the limit of detections.

Supplementary Table 2 – continuation

			Major element (wt.%)					Trace element (ppm)											
Rock type	Sample #	Host mineral	S	Fe	Co	Ni	Cu	Mn	Zn	As	Se	Mo	Pd	Pd corrected	Ag	Te	Pt	Au	Pb	Bi
Trachybasalt	BR-10	Al-, Ti-rich Cpx	50	49	0.15	1.06	0.17	(105)	(418)	(162)	(689)	(164)	(71.8)	(71.8)	(61.4)	(239.5)	0.6	6.6	105	(7.2)
Trachybasalt	BR-10	Al-, Ti-rich Cpx	55	44	0.11	0.37	0.08	1390	(232)	(100)	(376)	(73)	(48.1)	(48.1)	(26.7)	(106.4)	(4.9)	(5.1)	39	(3.6)
Trachybasalt	BR-10	Al-, Ti-rich Cpx	34	60	0.20	2.45	3.35	2158	333	(89)	(374)	(63)	6.8	6.7	9.3	(79.1)	(6.3)	(5.1)	26	(3.6)
Trachybasalt	BR-10	Al-, Ti-rich Cpx	48	47	0.17	1.64	3.20	218	(248)	(118)	(309)	(72)	(53.0)	(53.0)	(33.3)	(87.0)	(4.6)	(6.5)	39	(6.1)
Trachybasalt	BR-10	Al-, Ti-rich Cpx	52	44	0.17	1.75	2.77	(77)	(310)	(146)	(375)	(89)	(61.7)	(61.7)	17.5	(106.8)	(5.6)	(7.6)	(11)	(7.3)
Trachybasalt	BR-10	Al-, Ti-rich Cpx	35	62	0.16	0.38	2.41	1101	(146)	(55)	(351)	(38)	5.3	5.6	6.1	(43.5)	0.5	0.3	(6)	(2.6)
Basanite	BR-11	Al-, Ti-rich Cpx	27	62	0.18	1.50	9.95	(63)	393	144	(838)	(84)	15.3	12.5	325.9	(303.4)	3.5	14.5	456	(5.7)
Basanite	BR-11	Al-, Ti-rich Cpx	38	59	0.23	2.20	0.08	(56)	(276)	(123)	(820)	(30)	22.6	23.9	(28.5)	(139.9)	0.7	7.5	(7)	(2.6)
Basanite	BR-11	Al-, Ti-rich Cpx	35	63	0.11	0.70	1.63	5656	(525)	(285)	(1831)	(141)	10.7	11.3	1.0	(497.0)	(12.9)	0.9	(14)	(9.0)
Basanite	BR-11	Al-, Ti-rich Cpx	30	65	0.21	2.12	3.07	619	(418)	(305)	(1432)	(89)	(72.9)	(72.9)	(58.1)	(391.2)	(15.4)	6.2	(15)	(5.7)
Basanite	BR-11	Al-, Ti-rich Cpx	49	44	0.33	2.60	4.20	4213	(921)	(536)	(2492)	(316)	8.3	7.8	(113.9)	(879.0)	2.7	19.0	(29)	(14.6)
Basanite	BR-11	Al-, Ti-rich Cpx	36	59	0.22	1.86	2.54	130	(75)	(38)	(207)	(35)	4.8	5.0	148.0	(73.2)	(2.6)	6.2	338	(1.2)
Basanite	BR-11	Al-, Ti-rich Cpx	33	63	0.22	1.32	2.63	648	223	(89)	(534)	(38)	(23.4)	(23.4)	0.9	(104.7)	0.7	(4.4)	(4)	(1.7)
Basanite	BR-11	Al-, Ti-rich Cpx	40	60	0.10	(0.04)	0.83	1304	186	(103)	(488)	(44)	8.9	9.8	0.3	(150.5)	0.9	1.3	(4)	(2.3)
Basanite	BR-11	Al-, Ti-rich Cpx	37	61	0.18	0.37	1.58	943	169	(15)	74	(4)	(4.1)	(4.1)	3.9	(14.5)	0.1	0.0	1	(0.2)
Basanite	BR-11	Al-, Ti-rich Cpx	39	58	0.27	0.60	1.84	938	321	(14)	152	(15)	2.0	2.5	2.4	(49.0)	(1.0)	0.2	7	1.8
Basanite	BR-11	Al-, Ti-rich Cpx	39	59	0.20	0.52	1.68	(30)	153	(73)	(425)	(21)	(16.4)	(16.4)	(13.6)	(124.4)	(2.9)	(4.4)	(3)	(2.3)
Basanite	BR-11	Al-, Ti-rich Cpx	35	63	0.11	0.09	1.86	1204	387	(65)	(248)	(33)	5.7	6.3	(16.0)	(31.5)	(4.9)	(4.9)	(5)	(2.7)
Basanite	BR-11	Al-, Ti-rich Cpx	34	52	0.12	2.03	11.87	639	451	(88)	(513)	(76)	42.0	38.5	75.0	(87.2)	3.8	6.2	374	11.3
Basanite	BR-11	Al-, Ti-rich Cpx	30	66	0.12	(0.07)	3.77	401	(556)	(220)	(720)	(148)	19.9	19.6	2.9	(96.8)	0.4	11.2	(13)	(8.8)
Trachyandesite	BR-06	Amp	53	46	0.09	0.04	0.36	293	(223)	(67)	(376)	(46)	(39.4)	(39.4)	3.3	(59.2)	(2.0)	0.7	(3)	(1.6)
Trachyandesite	BR-06	Amp	55	44	0.08	(0.08)	0.18	(82)	(472)	(150)	(724)	(122)	0.1	1.3	(44.2)	(188.5)	(5.4)	(6.0)	(9)	(3.1)
Basaltic trachyandesite	BR-08	Amp	34	63	0.20	0.41	1.98	15707	(448)	(111)	(560)	(61)	5.2	5.7	(23.5)	(102.0)	1.8	1.5	(7)	(3.7)
Basaltic trachyandesite	BR-08	Amp	43	52	0.21	1.94	2.94	(321)	(1655)	(462)	(2083)	(322)	(242.7)	(242.7)	(91.3)	(686.7)	(39.6)	(29.7)	67	(23.8)
Basaltic trachyandesite	BR-08	Amp	46	50	0.19	1.01	2.69	(50)	(209)	(68)	(468)	(54)	(34.5)	(34.5)	(14.3)	(122.8)	(7.2)	(5.7)	(6)	(2.8)
Basaltic trachyandesite	BR-08	Amp	32	64	0.20	0.92	2.93	1565	(386)	(213)	1290	(56)	38.7	38.8	11.7	(326.6)	(11.7)	(8.9)	29	(4.0)
Basaltic trachyandesite	BR-08	Amp	41	56	0.23	0.83	2.21	(76)	(352)	(170)	(622)	(95)	(53.0)	(53.0)	8.2	(159.7)	1.5	(8.9)	(11)	(5.1)
Basaltic trachyandesite	BR-08	Amp	50	47	0.16	0.88	1.68	(68)	506	(185)	(780)	(72)	12.4	13.0	(35.3)	(120.1)	(6.5)	(7.0)	49	(3.4)
Basaltic trachyandesite	BR-08	Amp	49	48	0.20	1.10	1.87	98	354	(102)	(604)	(86)	(67.6)	(67.6)	(37.5)	(112.7)	0.0	4.1	30	(5.3)